This is a repository copy of *Digital Simulation and Discrete Modelling of a Chaotic System*.

White Rose Research Online URL for this paper:
http://eprints.whiterose.ac.uk/79297/

Monograph:

Billings, S.A. and Aguirre, L.A. (1992) Digital Simulation and Discrete Modelling of a Chaotic System. Research Report. ACSE Research Report 447 . Department of Automatic Control and Systems Engineering

eprints@whiterose.ac.uk
https://eprints.whiterose.ac.uk/

Digital Simulation and Discrete Modelling of a Chaotic System

S A Billings and L A Aguirre
Department of Automatic Control and Systems Engineering
University of Sheffield
P O Box 600
Mappin Street
Sheffield
S1 4DU

Digital Simulation and Discrete Modelling of a Chaotic System

Luis A. Aguirre   *Prof. Steve A. Billings*

Department of Automatic Control and Systems Engineering
The University of Sheffield
PO Box 600, Mappin Street - Sheffield S1 4DU - UK
e-mail: aguirre@uk.ac.shef.acse

ABSTRACT

The influence of the integration interval Δt of the fourth-order Runge-Kutta algorithm on Duffing's equation is investigated. Discretised models of the continuous equation are also derived and the effects of the discretisation period T on the discrete models is studied. Bifurcation diagrams and Poincaré maps are used to assess the accuracy of the results and it is shown that both these methods suggest smaller upper bounds for the integration interval and the discretisation period than other criteria.

Key words. Nonlinear modelling, Runge-Kutta simulation, chaotic systems

1. Introduction

The study of chaotic systems has received increasing attention over the last three decades. This period roughly coincides with a major expansion of the computer industry. Such a coincidence is not a surprise since some of the numerical tools required in the analysis of chaotic systems are very computer-demanding, thus the millions of iterations involved in the analysis of a chaotic system have been made feasible recently by modern digital computers.

When simulating continuous systems on such machines a numerical algorithm must be used to perform the integration. Three questions can then be asked: i) how should the integration interval, Δt, be chosen in order to obtain reliable results? ii) can the system be approximated by a discrete model which faithfully reproduces the nonlinear dynamics? and iii) if the answer to the latter question is affirmative, then how should the discretisation interval, T, be chosen?

Grantham and Athalye [1] worked on Lotka-Volterra equations and reported that the fourth-order Runge-Kutta algorithm may alter the system dynamics if Δt is not sufficiently small and that the second-order Runge Kutta qualitatively changes the system solutions even for fairly small values of Δt. Mallet-Paret and Nussbaum [2] have shown that a discrete approximation of a singularly perturbed delay continuous equation does not preserve the dynamical structure of the original system no matter how accurate the approximation is. They argue, however, that a faithful discrete version of the continuous system exists and can be obtained by other means.

The aforementioned papers suggest that the effects of the integration interval and the approximation procedure used in the derivation of discrete models is very system-dependent, and hence that this hampers the establishment of more general results. The present study aims to answer the three questions above for Duffing's equation. The answers themselves are, perhaps, not the most important results reported since it will be shown that the choice of Δt and T may prove inadequate even when a very good agreement at the *time-series-simulation* level is achieved. Bifurcation diagrams and Poincaré maps are used to assess the accuracy of the models in both regular and chaotic regimes and these reveal if the chosen values of Δt and T are adequate or not. Although the results reported are only based on Duffing's equation over a limited range of parameter values, the implications for other non-linear systems appears to be the same.

Some background material is presented in section 2. The results concerning the simulation of Duffing's continuous equation are presented in section 3. Discretised models for Duffing's equation are derived and validated in section 4. The main conclusions are summarised in section 5.

2. General background

2.1. Duffing's equation

Duffing introduced a nonlinear oscillator with a cubic stiffness term to describe the hardening spring effect observed in many mechanical systems. Since then Duffing's oscillator equation has become, together with van der Pol's equation, one of the commonest examples in nonlinear oscillation texts and research articles [3]. There are, however, two different types of equations: i) Duffing's non-linear inductor equation, used to model nonlinear electrical oscillators, and ii) Duffing's two-well potential equation, used to model the dynamics of a buckled elastic beam. In this work the former equation is considered and this can be expressed as

$$\ddot{x} + k\dot{x} + x^3 = f \cos\omega t \tag{1}$$

Hereafter constant values are assigned to k and ω, namely $k=0.1$ and $\omega=1$ rad/sec.

The nonautonomous equation above can be rewritten as an autonomous system at the expense of adding an extra state $\theta=\omega t$, thus

$$\dot{u} = v$$
$$\dot{v} = -0.1v - u^3 + f \cos\theta$$
$$\dot{\theta} = 1 \tag{2}$$

and $(u,v;\theta) \in R^2 \times S^1$.

2.2. Bifurcation diagrams

A useful tool for assessing the characteristics of the steady-state solutions of a system for a range of parameter values is the bifurcation diagram.

A point r of a bifurcation diagram of the kind used in this work is defined as:

$$r = \left\{ (x,f) \in R \times I \mid x=x(t_i),\ f=f_0;\ t_i=K_{ss}\times 2\pi/\omega \right\} \tag{3}$$

where I is the interval $I=(f_i,f_f) \subset R$ and K_{ss} is a constant.

In words, the point r as defined in (3), is chosen by simulating the system (1) for a sufficiently long time $K_{ss}\times 2\pi/\omega$ with $f=f_0$ and then plotting $x(K_{ss}\times 2\pi/\omega)$ against f_0. In practice, however, for each value of the parameter f, n_b points are taken at the instants:

$$t_i = (K_{ss}+ i) \times 2\pi/\omega \qquad i=0,1,...,n_b-1 \tag{4}$$

A bifurcation diagram will therefore reveal at which values of the parameter $f \in I$ the solution of the system bifurcates. Further, when studying chaos, such diagrams are useful in detecting parameter

ranges for which the system behaviour is chaotic. However, it has been pointed out [4] that these diagrams cannot distinguish between chaotic and quasiperiodic regimes and therefore first-return maps should also be consulted.

2.3. Poincaré or first-return maps

Consider a periodic orbit γ of some flow ϕ_t in R^n arising from a nonlinear vector field. Let $\Sigma \subset R^n$ be a hypersurface of dimension $n-1$ such that it is transverse to the flow ϕ_t. Thus the first return or Poincaré map $P = \Sigma \to \Sigma$ is defined for a point $q \in \Sigma$ by (see figure 1):

$$P(q) = \phi_\tau(q) \tag{5}$$

where τ is the time taken for the orbit $\phi_t(q)$ based at q to first return to Σ.

As mentioned earlier, equation (2) is the representation of (1) in a cylindrical state space $R^2 \times S^1$. Furthermore, as $\omega=1$, system (2) is periodic in θ with period 2π. Hence, the planes $\theta=0$ and $\theta=2\pi$ coincide and therefore provide a good choice for Σ, which is, for the purposes of the present work, chosen as

$$\Sigma = \left\{ (u,v;\theta) \in R^2 \times S^1 \mid \theta=0 \right\} \tag{6}$$

This is illustrated in figure 1.

The map defined in (5) is very useful in the analysis of nonlinear systems since it takes place in a space which is of lower dimension than the actual system. It is therefore easy to see that a fixed point of P corresponds to a periodic orbit of period $2\pi/\omega$ for the flow. Similarly, a subharmonic of period $l \times 2\pi/\omega$ will appear as l fixed points in P. Quasiperiodic and chaotic regimes can also be readily recognised using Poincaré maps. For instance, the first-return map of a chaotic solution is formed by a well-defined and finely-structured set of points for noise-free Hamiltonian systems.

More details concerning Poincaré maps may be found elsewhere [3-5].

3. Simulation of Duffing's equation

3.1. Time series

A fourth-order Runge-Kutta algorithm was used to carry out the integration of equation (1). The different values of the integration interval, Δt, were chosen as fractions of π in order to facilitate sampling the system exactly on Σ. If Δt were to be chosen in a different way, more sophisticated methods for obtaining the Poincaré maps would have to be used [6]. Figure 2 shows the system output $x(t)$ for $f=6.5$ and $\omega=1$ rad/sec when the system is simulated using $\Delta t = \pi/3000$; $\pi/600$; $\pi/300$ and $\pi/125$. The responses are virtually indistinguishable up to plotting precision and this would therefore suggest that

all the values of Δt are acceptable.

3.2. Bifurcation diagrams

The bifurcation diagrams of system (1) for various values of Δt were obtained as outlined in section 2.2. In all cases the parameter f was varied in the range $4.5 \leq f \leq 12$, i.e. $I=(4.5,12)$ and $K_{ss}=400$, $n_b=50$ for chaotic regimes and $n_b=6$ otherwise. Several bifurcation diagrams were obtained simulating the system with different values of Δt. Figures 3a-3d correspond to $\Delta t = \pi/3000$; $\pi/600$; $\pi/300$; $\pi/125$ respectively. If Δt is increased beyond $\pi/30$ the integration procedure becomes unstable.

Some of the bifurcation points in the diagrams are labelled B1 to B9 as shown in figure 3a. Some steady-states shown in figure 3a can roughly be classified as follows. From $f=4.5$ to $f=$B1 a period-1 regime is observed. From B1 to B2 a period-2 and from B2 to B3 a period-4. The system displays chaos for $f=$B3 up to B4 when a period-3 is established. Period-3 regimes are observed up to B7 where each solution period-doubles and again at B8, i.e. just after B8 a period-12 can be verified. For the sake of simplicity, it is assumed that the system is driven into chaos at B8 (this actually happens just after B8) and returns to a period-1 at B9.

Remark 1. B1→B2→B3 and B7→B8 are period-doubling cascades which are a well known route to chaos and follow a well-defined invariant pattern [7].

Remark 2. Ueda [8] has presented a $k \times f$ chart (N.B. here k=0.1) generated by digital and analogue computers (the same chart can be also found in reference [4] page 158). The agreement of figure 3a with Ueda's analogue results is striking. It should be stressed, however, that slight differences occur and can be explained based on the selection of initial conditions. For instance, for k=0.1 and $11.6 \leq f \leq 13.4$ chaotic or period-1 steady-states can take place depending on the initial conditions used. In the present work the following initial conditions were always chosen $x(0)=0$ and $\dot{x}(0)=0$.

It is clear from figures 3a-3d that the bifurcation diagrams and consequently the nonlinear phenomena involved change significantly as Δt is increased. For instance, the bifurcation diagram of figure 3b displays what was named an unfinished period-doubling cascade [4]. Further, as Δt is increased the aforementioned cascade will eventually terminate in a chaotic regime in the range $7.2 \leq f \leq 7.7$ as shown in figure 3c. Poincaré maps verify that the system does not settle to a single period-3 regime in the range $8 \leq f \leq 9.5$ but rather period-1 attractors are also observed, for instance at $f=8.95$. Figure 3d shows that the system behaviour degrades further as Δt is encreased, although it still exhibits some features associated with the *original* diagram for low values of f.

Figure 4 illustrates how Δt affects the bifurcation points. Disrupted lines indicate that the corresponding bifurcation point is not clearly observed in the respective diagram. From the figure it can

be inferred that Δt does not strongly affect the values of f at which the system bifurcates, although the way the system bifurcates is very different for large values of Δt.

Grantham and Athalye [1] have reported that for the Lotka-Volterra equations the fourth-order Runge-Kutta algorithm may introduce chaotic regimes for insufficiently small values of Δt and that the second-order Runge-Kutta may provoke chaos even for very small values of Δt. Similar results for Duffing's equation can be observed for the fourth-order Runge-Kutta algorithm from figures 3c and 3d.

Although the system displays chaos approximately in the same ranges of values of f ($5.6 \leq f \leq 5.8$ and $10 \leq f \leq 11.6$) for $\Delta t = \pi/3000$; $\pi/600$; $\pi/300$, but this does not necessarily mean that the chaotic regimes in each case possess the same characteristics. In order to gain further knowledge of such regimes, Poincaré maps will now be used.

3.3. Poincaré maps

Figures 5a and 5b display the Poincaré maps for $\Delta t = \pi/3000$ with $f=5.7$ and $f=11$ respectively. Poincaré maps of chaotic attractors of Duffing's equation can be found elsewhere (see for instance reference [4] page 86) and a very good agreement can be observed. Slight differences can be explained based on the different values of f and k. Figures 5a and 5b will therefore be referred to as the *uncorrupted* maps for Duffing's equation.

Figures 6a-6c show the Poincaré maps for $f=11$ and $\Delta t = \pi/600$; $\pi/300$; $\pi/125$ respectively. The main differences observed are of twofold: i) fuzziness, as Δt is increased some of the fine structure is lost, this can be quantified by the fractal dimension [9,10], and ii) position, the attractor occupies a different position in the state space (see the marked point in the figures). The attractor for $\Delta t = \pi/125$ is quite different as expected from the bifurcation diagrams.

It should be emphasised that although the chaotic regimes for $\Delta t = \pi/3000$; $\pi/600$; $\pi/300$ occur approximately for the same values of f, the Poincaré maps have exposed some differences. In particular, consider the bifurcation diagrams of figures 3a and 3b which are virtually indistinguishable over the ranges for which chaotic motions are observed. Nevertheless, the attractors shown in figures 5b and 6a reveal that some dynamic aspects of the system are still affected by Δt in the range $\pi/3000 \leq \Delta t \leq \pi/600$. Similar results hold for the attractors found at $5.5 \leq f \leq 5.8$.

The results of the present section have illustrated the effects of varying the integration interval of the fourth-order Runge-Kutta algorithm on some nonlinear phenomena displayed by Duffing's equation. Further, the above results suggest that a suitable value for Δt would be $\pi/3000$. In what follows such a value will be employed to generate data which will be used to validate discretised versions of (1).

4. Discrete models for Duffing's equation

Discrete versions of equation (1) can be obtained using the following approximations:

$$\dot{x}(k) \simeq \frac{x(k+1) - x(k)}{T} \tag{7}$$

and

$$\dot{x}(k) \simeq \frac{x(k) - x(k-1)}{T} \tag{8}$$

respectively known as explicit Euler of forward difference and implicit Euler or backward difference approximations.

Using (7) and (8) in (1) two slightly different discrete versions of Duffing's equation can be readily obtained. The models using Euler's approximation are not globally stable, that is for some input amplitudes they become unstable and consequently such models are not considered here. Further, in order to be able to sample the solutions exactly on Σ when generating Poincaré maps, T was chosen as a fraction of π.

Using equation (8) and the approximation $x(k)^3 \simeq x(k-1)^3$ to avoid applying a predictor corrector method, models of the following form are obtained:

$$x(k) = \alpha x(k-1) + \beta x(k-2) + \gamma x(k-1)^3 + \delta u(k) \tag{9}$$

The model coefficients for different values of T are listed in Table 1.

TABLE 1 Coefficients of the Discretised Models

T	α	β	γ	δ
π:300	1.99895	-0.99895	-1.09547e-4	1.09547e-4
π:60	1.99479	-0.99479	-2.72727e-3	2.72727e-3
π:30	1.98963	-0.98963	-1.09547e-2	1.09547e-2
π:15	1.97948	-0.97948	-4.29650e-2	4.29650e-2
π:12.5	1.97548	-0.97548	-6.16168e-2	6.16168e-2

These models will be compared to the original system integrated with $\Delta t = \pi/3000$ in order to verify the influence of T upon them.

4.1. Time series and correlation functions

Figure 7 shows simulation data for $f=6.5$, $\Delta t=\pi/3000$ and the discretised models for $T=\pi/300$; $\pi/60$ and $\pi/30$. The responses are undistinguishable up to plotting precision. Further, the data obtained for $T=\pi/15$ and $\pi/12.5$ are very similar to those of figure 7 but appear out of phase. Although such a shift in time is obvious in a simulation context, in an application situation these responses could be incorrectly regarded as acceptable. Nevertheless, these results would suggest $T\approx\pi/30$ as an appropriate choice.

For comparison purposes, two other criteria were used to evaluate appropriate values for T. Considering $\tau_{min}/20 \leq T \leq \tau_{min}/10$ where τ_{min} is the time related to the first local minimum of the autocorrelation function of the response [11], values in the range $\pi/36 \leq T \leq \pi/17$ are found. Furthermore, choosing $1/T$ to be 10 times larger than the fastest peak in the signal power spectrum, suggest that $T\approx\pi/38$ would be appropriate. In this case the signal used was the system response for $f=11$ which is chaotic thus presenting a noise-like power spectrum.

Billings and Voon [12-13] have introduced high-order correlation functions to detect the presence of unmodelled terms in the residuals of discrete models. Thus if a model of a system is adequate the following conditions should hold

$$\Phi_{\varepsilon\varepsilon}(\tau) = E[\varepsilon(t-\tau)\varepsilon(t)] = \delta(\tau)$$

$$\Phi_{u\varepsilon} = E[u(t-\tau)\varepsilon(t)] = 0, \quad \forall\tau$$

$$\Phi_{u'^2\varepsilon}(\tau) = E[(u^2(t-\tau)-\overline{u^2}(t))\varepsilon(t)] = 0, \quad \forall\tau$$

$$\Phi_{u'^2\varepsilon^2}(\tau) = E[(u^2(t-\tau)-\overline{u^2}(t))\varepsilon^2(t)] = 0, \quad \forall\tau$$

$$\Phi_{\varepsilon(\varepsilon u)}(\tau) = E[\varepsilon(t)\varepsilon(t-1-\tau)u(t-1-\tau)] = 0, \quad \tau\geq0 \tag{10}$$

where ε are the residuals, defined as the difference between the actual measured output and the one-step-ahead predicted output, $u(t)$ is the input, the over-bar signifies the mean value and $E[.]$ indicates the mathematical expectation of the argument.

Such tests were used in the present study to assess the validity of the various discretised models. In what follows the output of the continuous model simulated with $\Delta t=\pi/3000$ was used as the benchmark measured data and the discretised models were used as predictors. A low amplitude noise was added to the data obtained from the continuous model in order to avoid numerical problems when computing the correlation functions and to simulate a more realistic scenario.

Figures 8a-8c show the correlation functions for models discretised with $T=\pi/12.5$; $\pi/15$ and $\pi/30$ respectively and figures 9a-9c depict the measured data superimposed on the predictor outputs. The

plots for $T=\pi/60$ and $\pi/300$ are even better than the ones for $T=\pi/30$ and are therefore omitted.

Care must be taken when using predictors for validating models which are sensitive to initial conditions since there is an uncertainty in the knowledge of the actual initial conditions due to the presence of noise and therefore the predictors will not be initialised with accurate data. Thus even a good model which is not properly initialised is likely to give a totally different response which will be judged unacceptable. In the present work the noise was not added to the first data points and consequently the predictors were initialised with accurate initial conditions. In practice the initial points may require some degree of smoothing to achieve the same objective.

From figures 9a-9c it is clear that although the predictors seem to perform fairly well, the correlation functions reveal that the models for $T=\pi/15$ and $\pi/12.5$ are inadequate. These results seem to suggest $T=\pi/30$ as an acceptable value for the discretising period.

The autocorrelation function of the residuals, $\Phi_{\varepsilon\varepsilon}$, of all the models are outside the 95% confidence bands at the lag $\tau=1$ because no noise model was fitted. The correlations $\Phi_{u\varepsilon}$, $\Phi_{\varepsilon(\varepsilon u)}$, $\Phi_{u^2{}'\varepsilon}$ and $\Phi_{u^2{}'\varepsilon^2{}'}$ indicate that the process model is adequate for $T\leq\pi/30$.

It is worth pointing out that the above results are in agreement and point to a discretisation period in the range $\pi/38\leq T\leq\pi/17$. However, in the next two sections it will be seen that T must be decreased further in order to yield a discretised model capable of faithfully reproducing the nonlinear phenomena.

4.2. Bifurcation diagrams

The bifurcation diagrams for $T=\pi/300$; $\pi/60$; $\pi/30$; $\pi/15$ and $\pi/12.5$ shown in figures 10a-10e respectively, were obtained following the same procedure as in section 3.2. If T is increased beyond $\pi/12.5$ unstable models are obtained. As figures 10a and 10b are quite similar, T was not further decreased. The bifurcation points were labelled as for the continuous diagrams and a very good agreement is observed between the diagram of figure 3a and those of the discretised models for small values of T.

The diagrams of figures 10d and 10e are clearly different. The model discretised with $T=\pi/15$ displays regular motions for $f\approx 10.7$, this is a unique feature of this model. As in the continuous case, larger values of T induce an extra chaotic regime in this case at approximately $6.6\leq f\leq 8.0$.

The chaotic window observed for the lower values of f is wider for models discretised using a small T. This narrowing of the chaotic window was not observed in the continuous case.

From figure 11 it can be seen that the bifurcation points of the discrete models are shifted to the left (with the exception of $B5$), in other words they happen at lower values of f as T is increased. In figure 12, the bifurcation points of figure 11 are compared with those of the continuous system obtained using $\Delta t=\pi/3000$. Thus from figure 12 an upper bound for T can be suggested, namely

$T \leq \pi/60$.

4.3. Poincaré maps

Figures 13a-13e show the Poincaré maps for $T=\pi/300$; $\pi/60$; $\pi/30$; $\pi/15$ and $\pi/12.5$ with $f=11$ ($f=10$ was used for $T=\pi/12.5$ only). As T is increased two main changes are observed: i) the original attractor becomes deformed, and ii) ghost attractors appear. To some extent these changes contrast with those observed in the continuous case, where ghost attractors did not happen, but the maps gradually lost some of the fine structure and therefore became fuzzier. However, such increase in fuzziness could be induced by the appearance of a ghost attractor, see for instance figure 6b where arrows indicate what seems to be the *original* attractor and an *underlying* one. Figure 6b is very similar to figure 13a although the latter is not as fuzzy as the former and it is better placed in the state space (see the coordinates of the indicated point).

One of the differences between the attractors of figures 6b and 13a is that the former seems to display the *original* attractor with most of the points on it, plus an *underlying* attractor with fewer points. Figure 13a displays two coexisting attractors with approximately the same number of points on each one.

Remark 1. It is interesting to note that for some discretised models two different, well-defined and finely-structured attractors coexist, see for instance figure 13d. Thus the increase in T does not only contribute for the deformation of the original attractor but also provokes the appearance of another one.

Remark 2. In some cases it was noted that the first set of points ($\approx 10,000$) lay on one attractor and suddenly the system "switched" to the second attractor. It was then appropriate to consider if the continuous simulation or discrete models with small T would also switch to another attractor for larger simulation times. Such models were therefore simulated for longer periods but no change was observed in their return maps.

Remark 3. Some discretised models do not switch suddenly from one attractor to another, rather the maps of both attractors are simultaneously formed as the system is simulated.

Figure 14 shows the Poincaré map of the discretised model for $T=\pi/600$. Comparing this figure to figure 13a it is clear that the ghost-effect is reduced, thus these figures suggest $T \leq \pi/600$ as an upper bound for the discretisation period which is much lower than the ones suggested by the criteria of section 4.1. Increasing the values of Δt and T yields models which take longer to settle to a steady-state regime. Indeed, if Δt and T are taken beyond their respective critical values unstable models arise which can be considered, in a sense, to take an infinite time to reach steady-state. It could therefore be argued that the extra chaotic window in the bifurcation diagrams appear because the models were not

in steady-state by the time the points in the diagram were taken. Poincaré maps, however, have revealed that in such cases the models display genuine chaotic behaviour.

5. Conclusions

The dynamical effects of the integration interval, Δt, of the fourth-order Runge-Kutta algorithm and the discretisation period, T, used in the derivation of discrete models for Duffing's equation have been investigated.

The main results can be summarised as follows:

a) Both Δt and T have strong effects on the dynamical behaviour of the considered models

b) Most of the effects are not clearly evident from the simulated time-series. However bifurcation diagrams and Poincaré maps were shown to be more sensitive to such effects and therefore suitable for validating the considered models

c) The increase in Δt and T affects the respective models in different ways. For example, increasing Δt induces new chaotic regimes which are observed in the bifurcation diagrams and also increases the fuzziness of the strange attractors revealed in the respective Poincaré maps. On the other hand increasingly large values of T shift the bifurcation points in the diagrams to the left, so that the models become chaotic for smaller input amplitudes. This also narrows the range of values at which chaotic regimes are observed. Models discretised with large T also present *new* strange attractors which coexist with the *original* attractor.

The use of bifurcation diagrams and Poincaré maps has revealed that smaller values of Δt and T should be used in order to yield reliable results. It is not being argued that the smaller Δt and T are the better, since such an assertion is obvious. What has been emphasised, however, is that the use of bifurcation diagrams and Poincaré maps suggest much smaller upper bounds for Δt and T than other criteria.

Acknowledgments

References

[1] Grantham, WJ and Athalye, AM. Discretization chaos: Feedback control and transition to chaos, in *Control and Dynamic Systems - Advances in Theory and Applications*, Academic Press Inc., Ed. by C.T. Leondes, vol. 34, part 1, pp. 205-277. 1990.

[2] Mallet-Paret, J and Nussbaum, RD. A bifurcation gap for a singularly perturbed delay equation, in *Chaotic dynamics and fractals*, ed. by M.F. Barnsley and S.G. Demko, Notes and Reports in

Mathematics in Science and Engineering, vol. 2, Academic Press Inc., Orlando, pp. 263-286. 1986.

[3] Guckenheimer, J and Holmes P. Nonlinear oscillations, dynamical systems, and bifurcation of vector fields, Springer-Verlag, New York, 1983.

[4] Moon, FC. Chaotic Vibrations - an introduction for applied scientists and engineers, John Willey and Sons. 1987.

[5] Parker, TS and Chua, LO. Chaos: a tutorial for engineers, *Proceedings of the IEEE* , vol. 75, no. 8, pp. 982-1008. 1987.

[6] Hénon, M. On the numerical computation of Poincaré maps, *Physica 5D*, pp. 412-414. 1982.

[7] Feigenbaum, MJ. Universal behaviour in nonlinear systems, *Physica 7D*, pp. 16-39. 1983.

[8] Ueda, Y. Steady motions exhibited by Duffing's equation: A picture book of regular and chaotic motions, in *New approaches to nonlinear problems in dynamics*, SIAM, Ed. by P.J. Holmes, pp. 311-322. 1980.

[9] Farmer, JD and Ott, E and Yorke, JA. The dimension of chaotic attractors, *Physica 7D*, pp. 153-170. 1983.

[10] Grassberger, P and Procaccia, I. Characterization of strange attractors, *Physical Review Letters*, vol. 50, no. 5, pp. 346-349. 1983.

[11] Abarbanel, HDI and Brown, R and Kadtke, JB. Prediction in chaotic nonlinear systems: Methods for time series with broadband Fourier spectra, *Physical Review A*, vol. 41, no. 4, pp. 1782-1807. 1990.

[12] Billings, SA and Voon, WSF. Structure detection and model validity tests in the identification of nonlinear systems. *IEE Proceedings*, vol. 130, Pt. D, no. 4, pp. 193-199. 1983.

[13] Billings, SA and Voon, WSF. Correlation based model validity tests for non-linear models. *Int. J. Control*, vol. 44, no. 1, pp. 235-244. 1986.
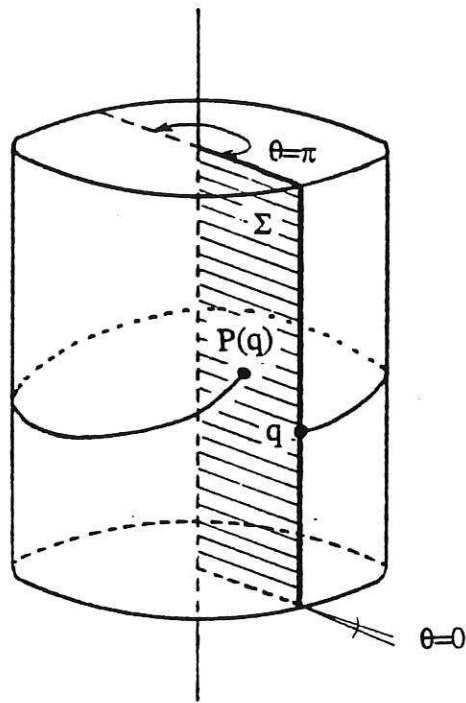
Figure 1. Representation of the Poincaré plane Σ in the Cylindrical state space of equation (2)
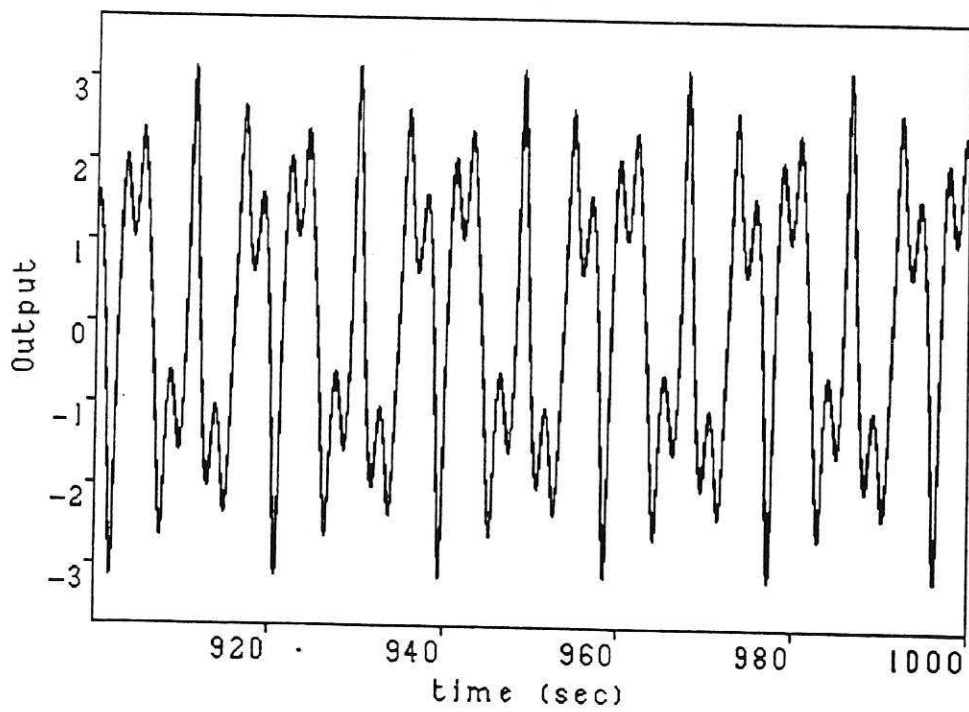
Figure 2. System output
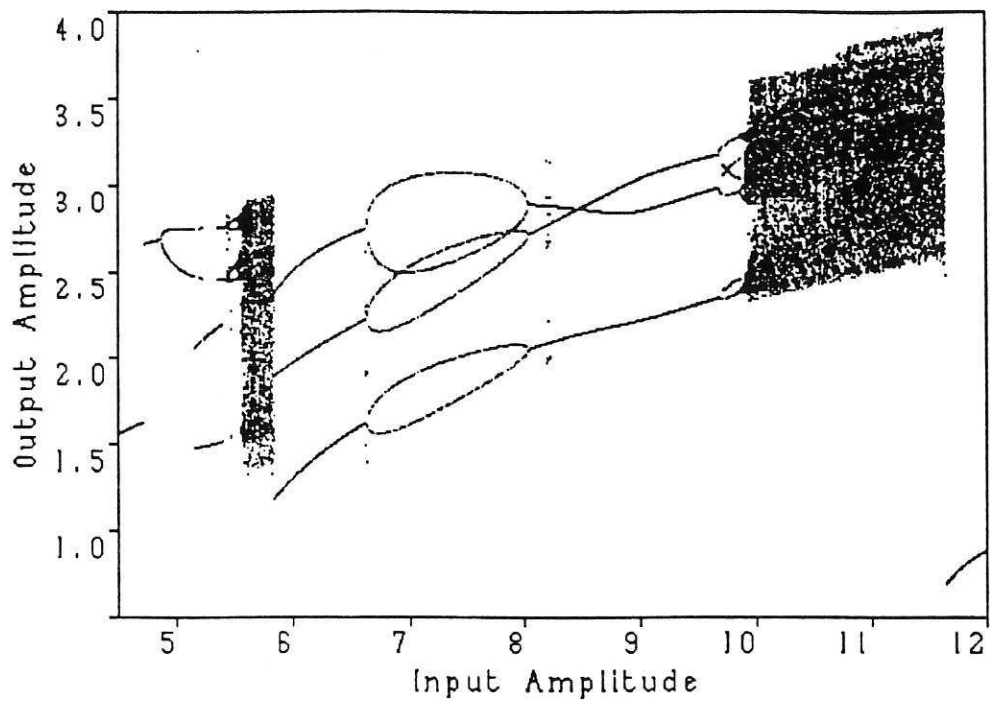
Figure 3a. Bifurcation Diagram $- \Delta t = \pi /3000$
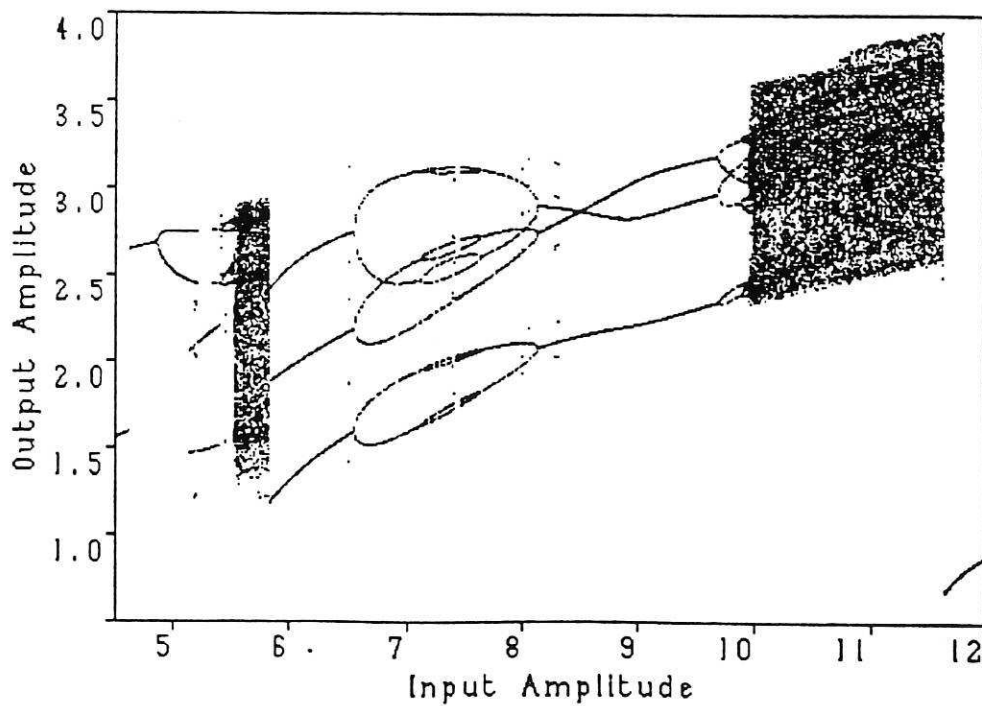
Figure 3b. Bifurcation Diagram $- \Delta t = \pi /600$
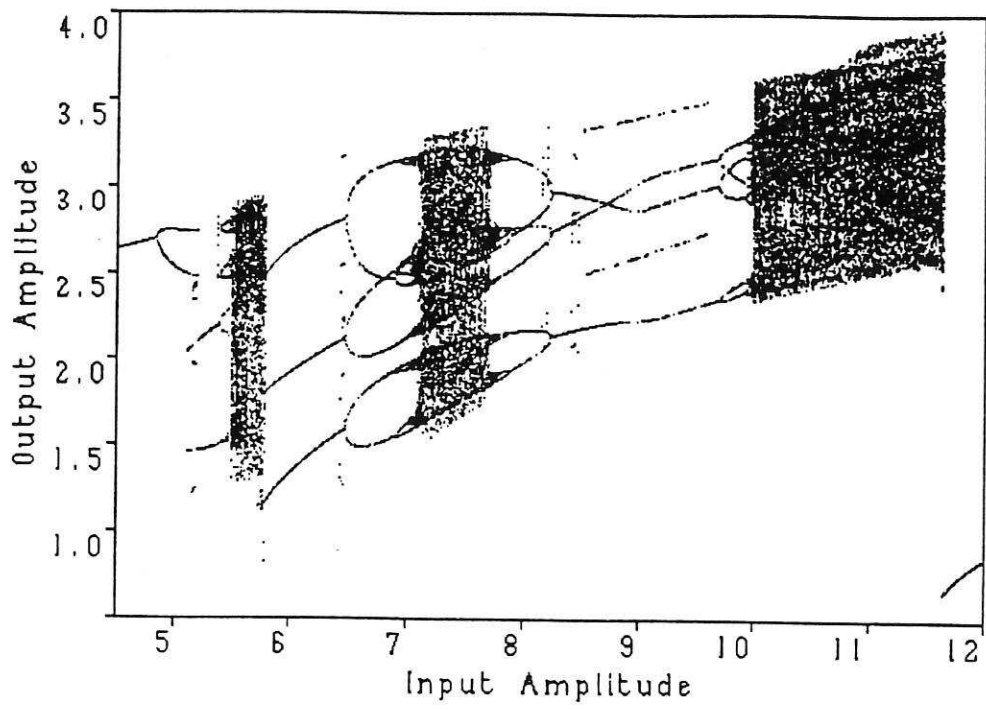
Figure 3c. Bifurcation Diagram – $\Delta t = \pi/300$
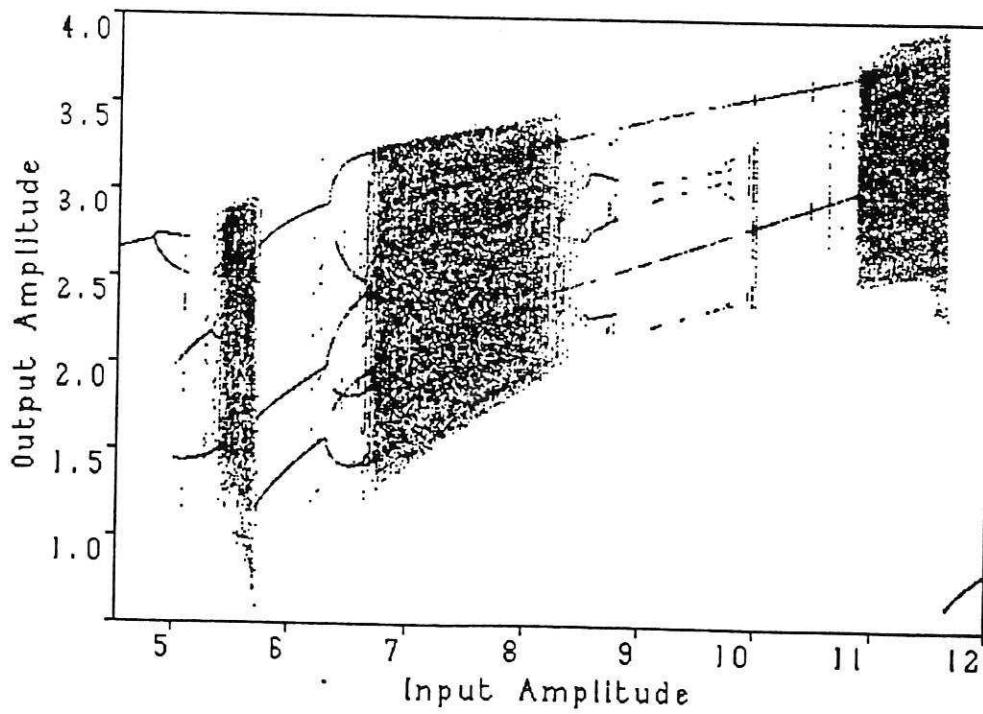
Figure 3d. Bifurcation Diagram – $\Delta t = \pi/125$
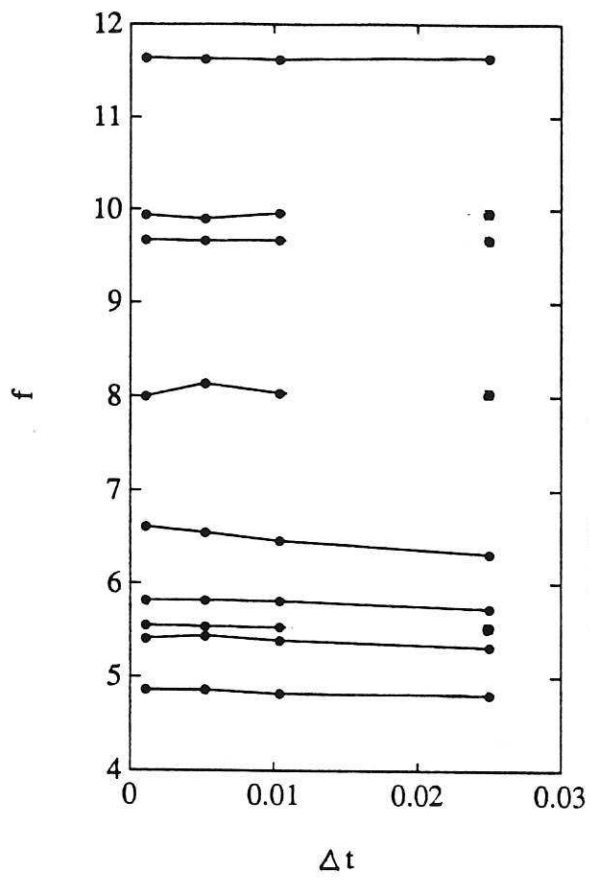
Figure 4. Influence of Δt on the bifurcation points

Figure 5a.   Poincaré Map — $\Delta t = \Pi/3000$, $F=5.7$

(1.38, 3.07)
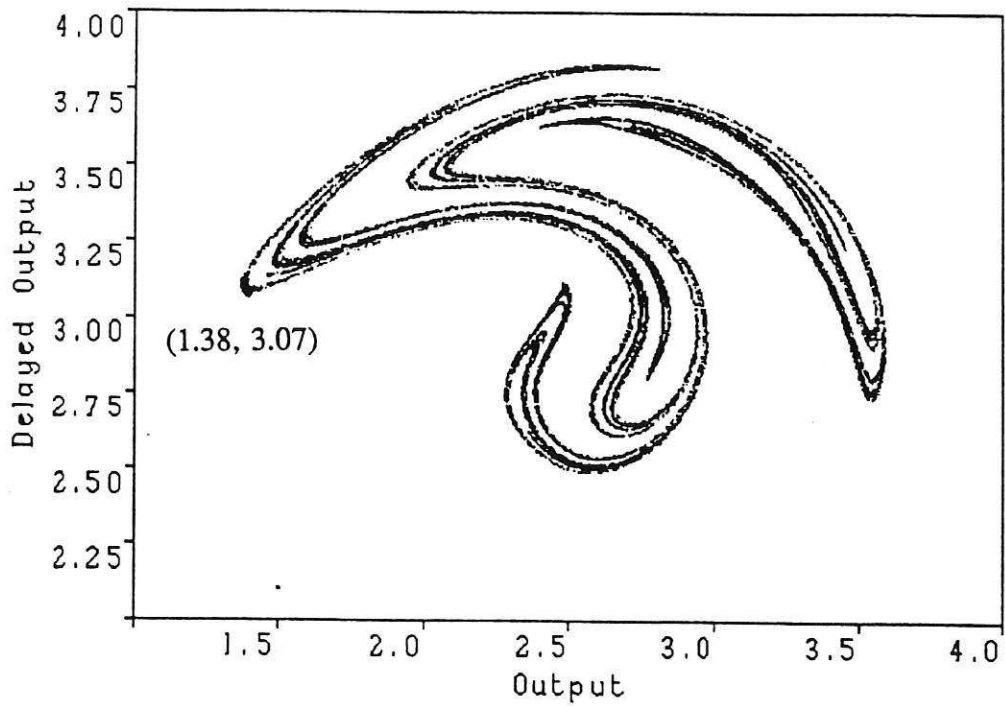
Figure 5b.   Poincaré Map — $\Delta t = \Pi/3000$, $F=11$

(1.37, 3.05)
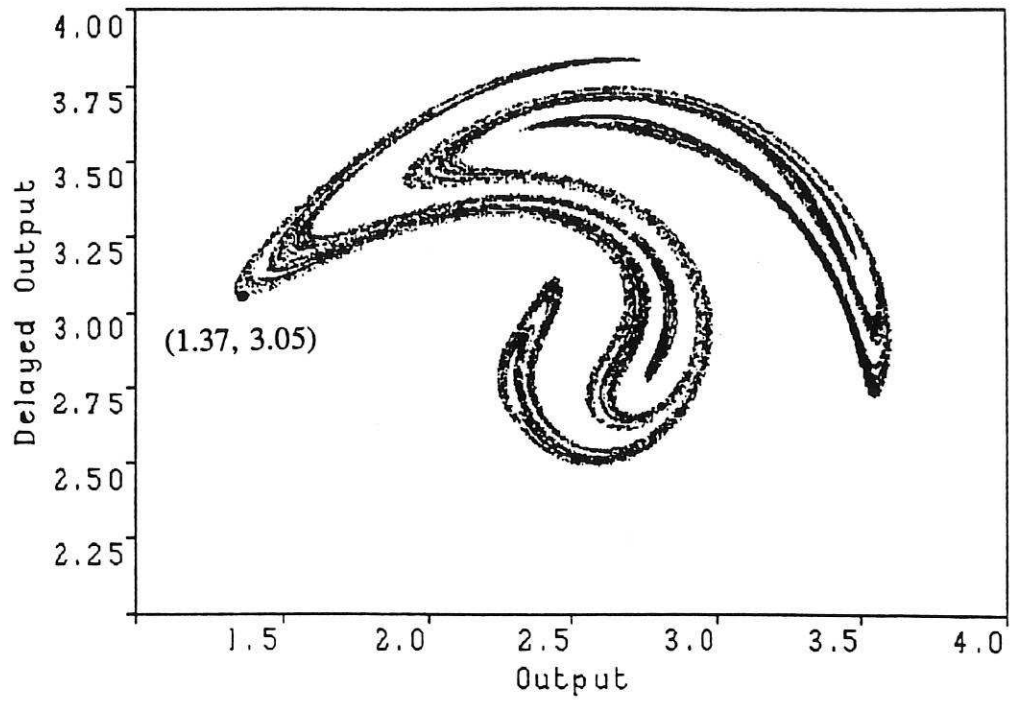
Figure 6a. Poincaré Map — $\Delta t = \pi/600$

(1.33, 3.02)
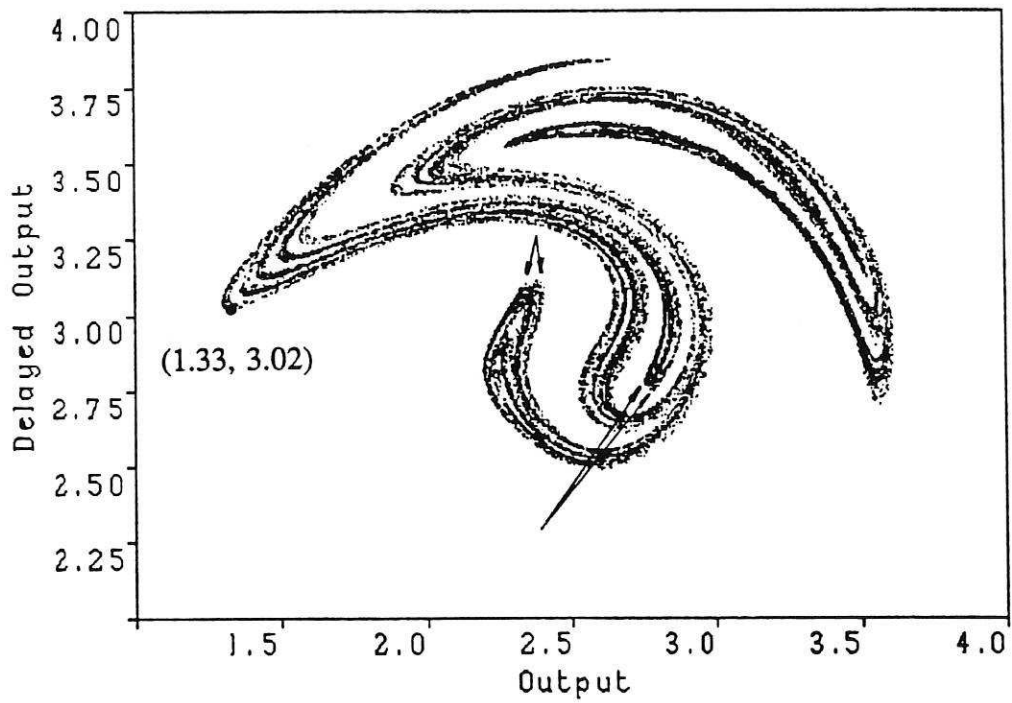
Figure 6b. Poincaré Map — $\Delta t = \pi/300$
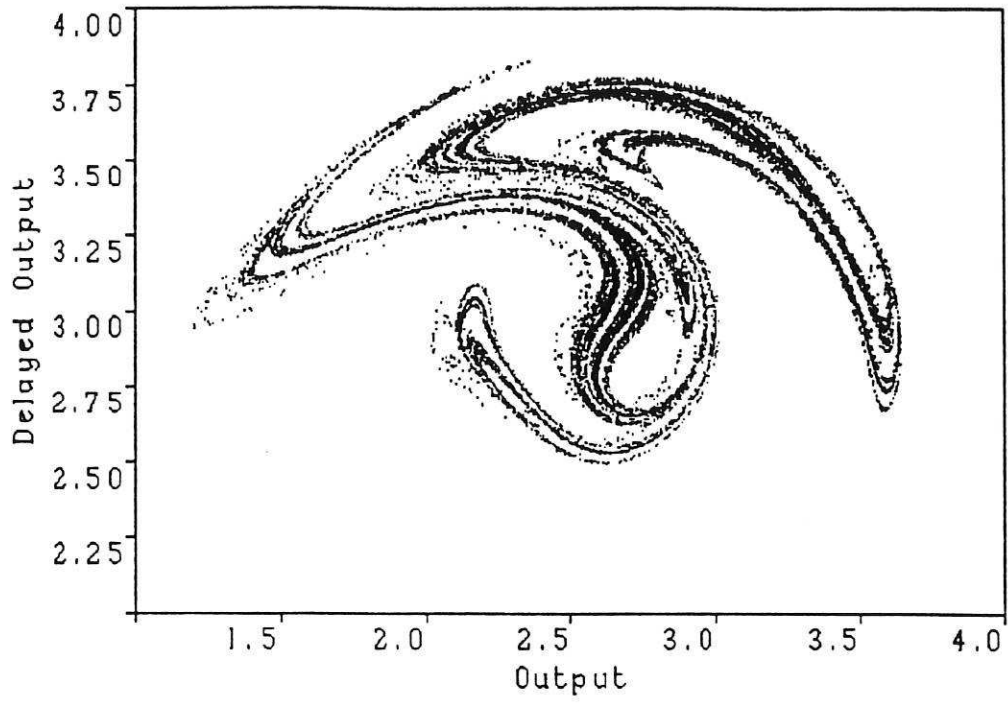
Figure 6c. Poincaré Map — $\Delta t = \Pi / 125$
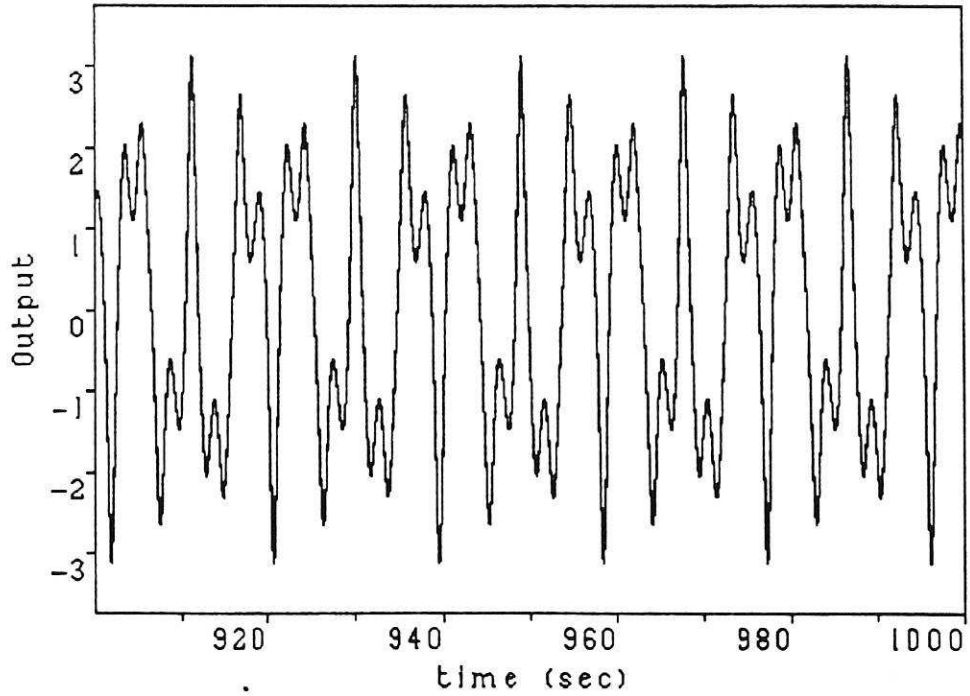
Figure 7. System output
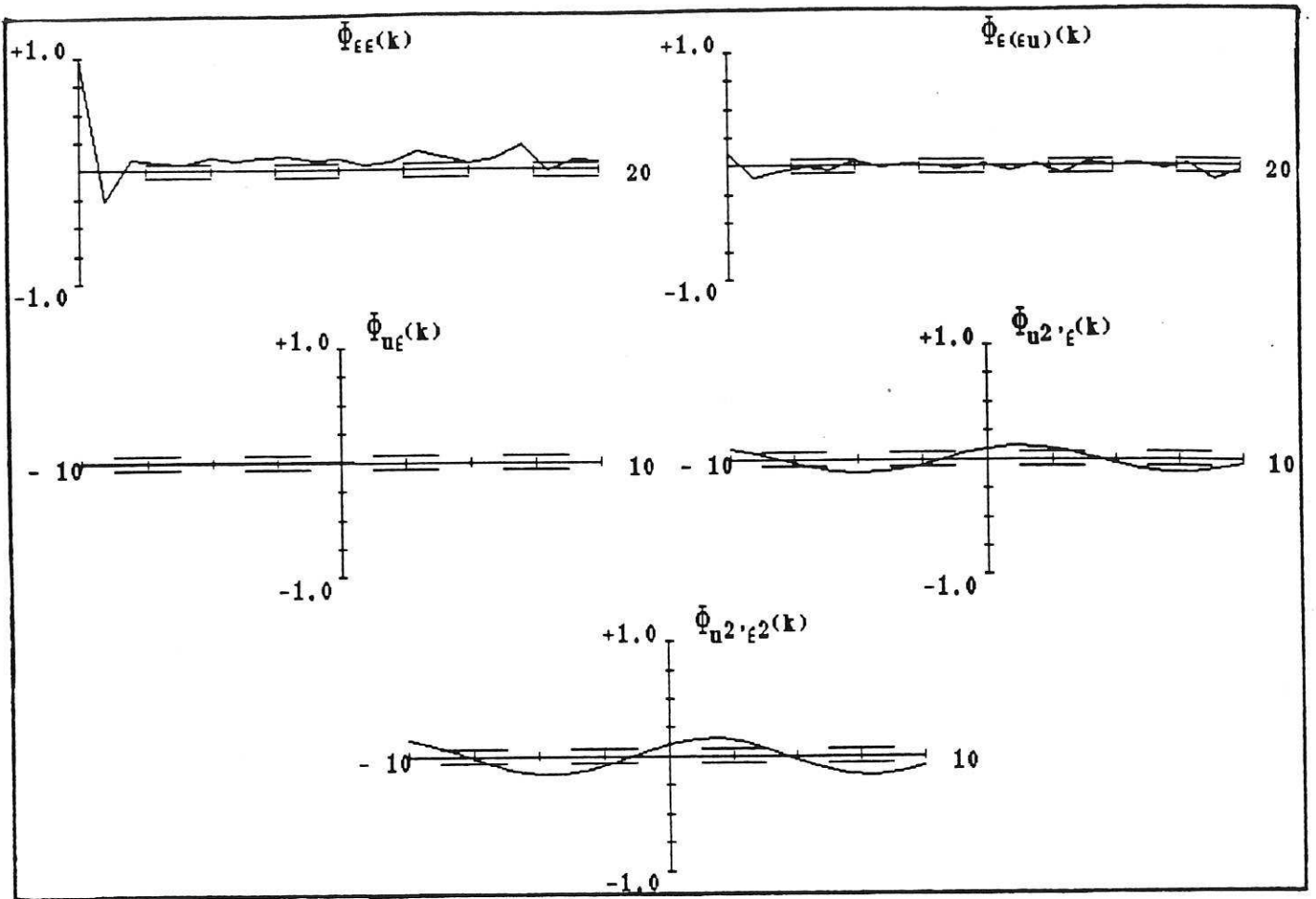
Figure 8a. Correlation functions - $T = \pi/12.5$
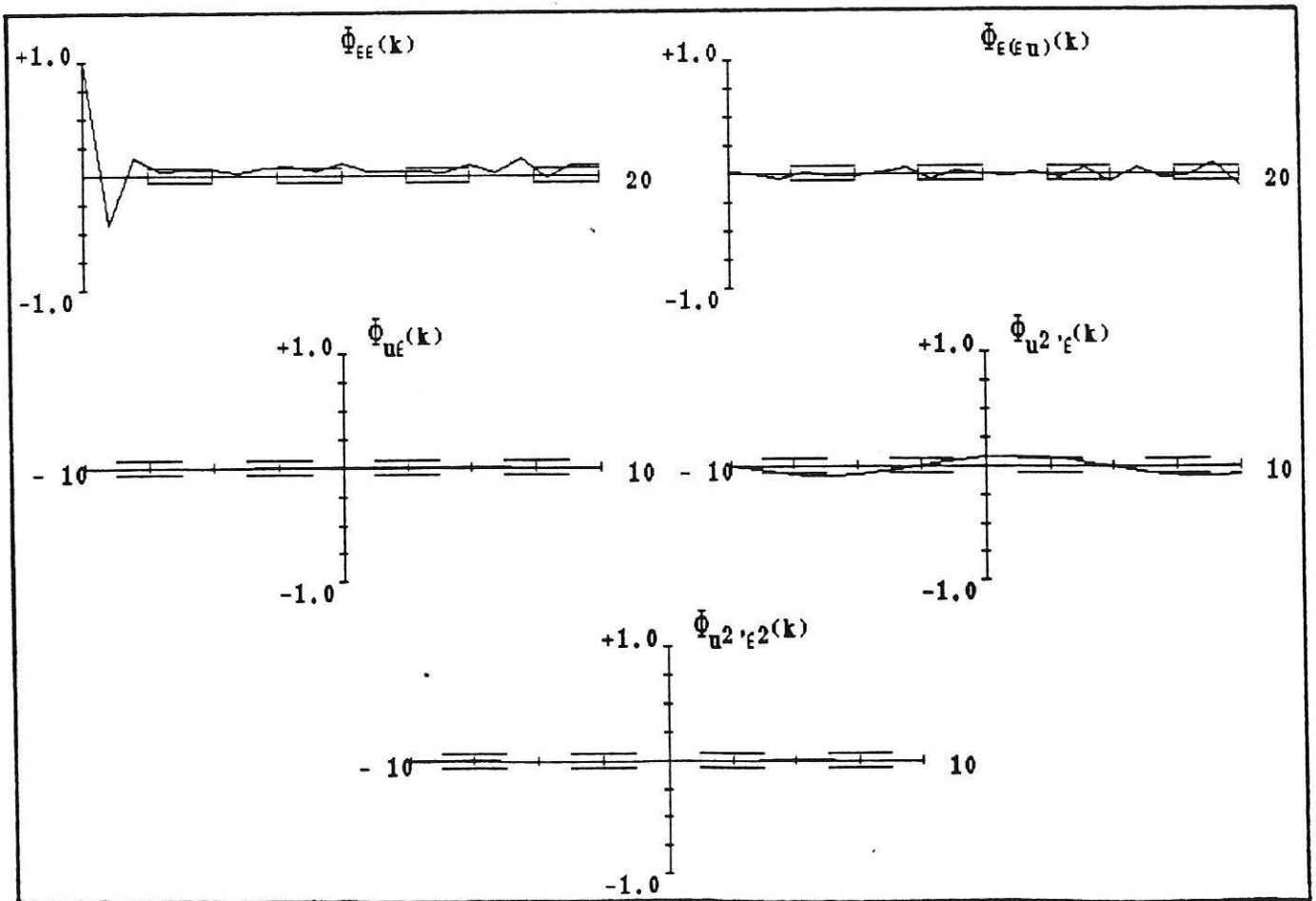
Figure 8b. Correlation functions - $T = \pi/15$
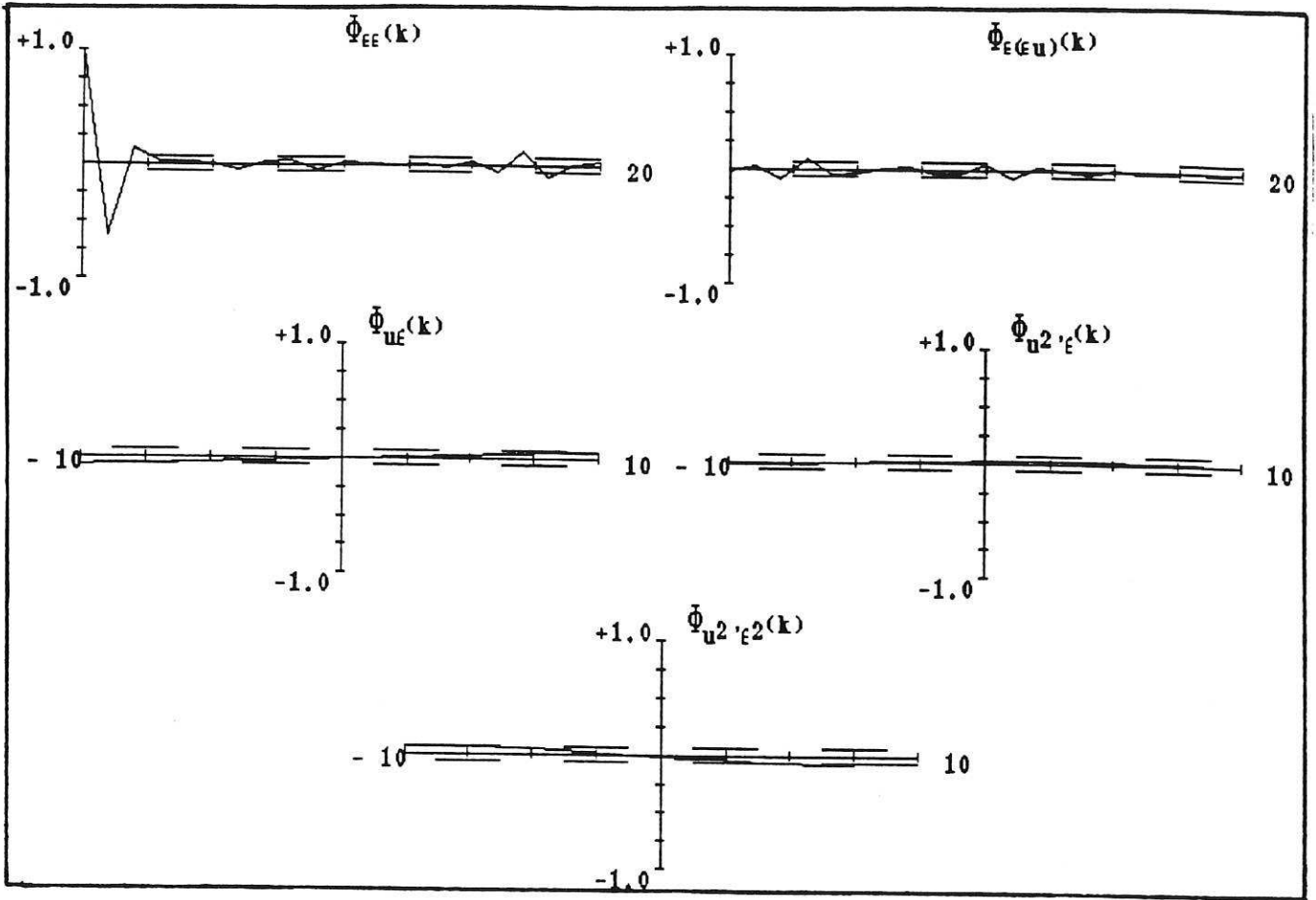
Figure 8c. Correlation functions - $T = \pi/30$
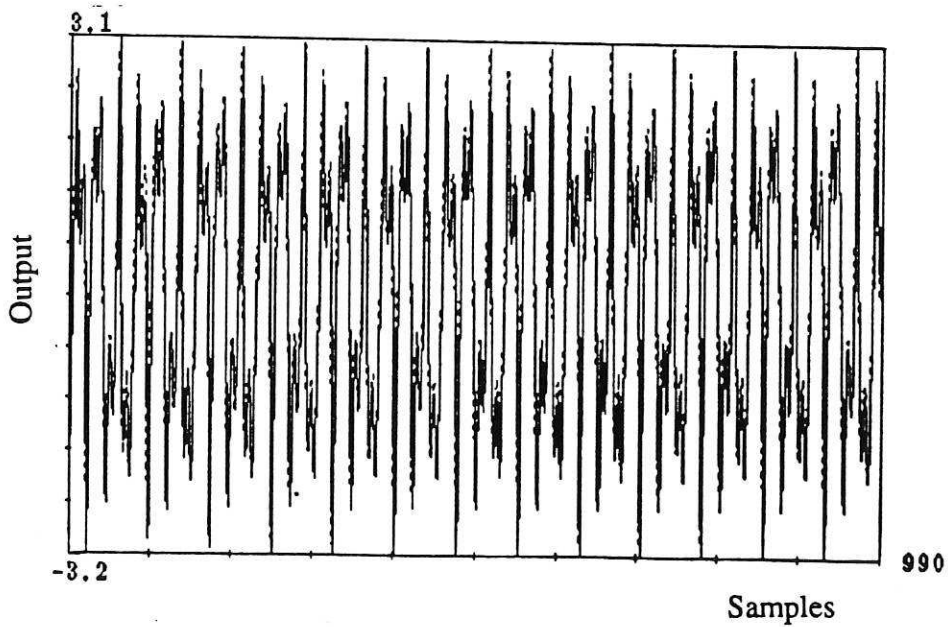
Figure 9a. (...) Measured output and (—) predicted output - $T = \pi/12.5$
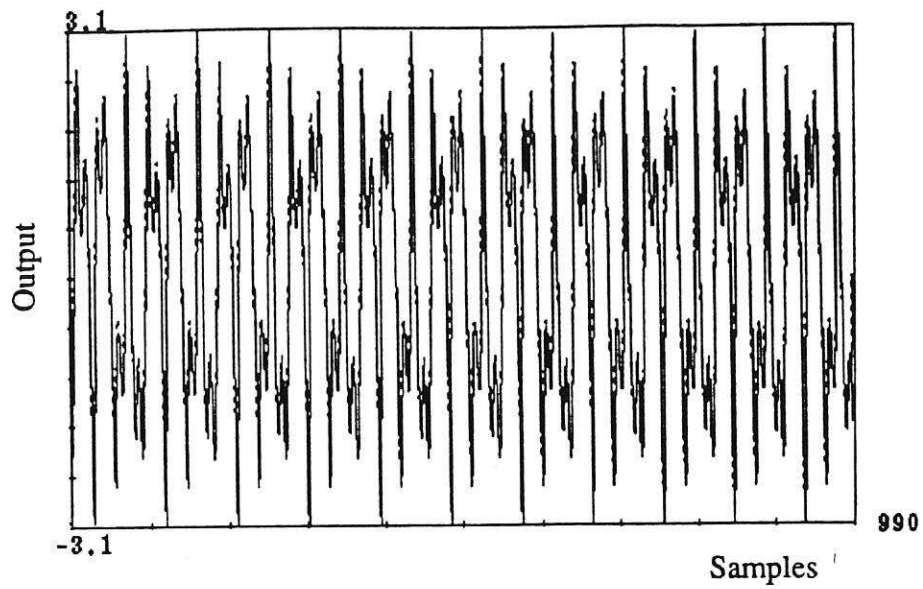
Figure 9b. (...) Measured output and (—) predicted output - $T = \pi/15$
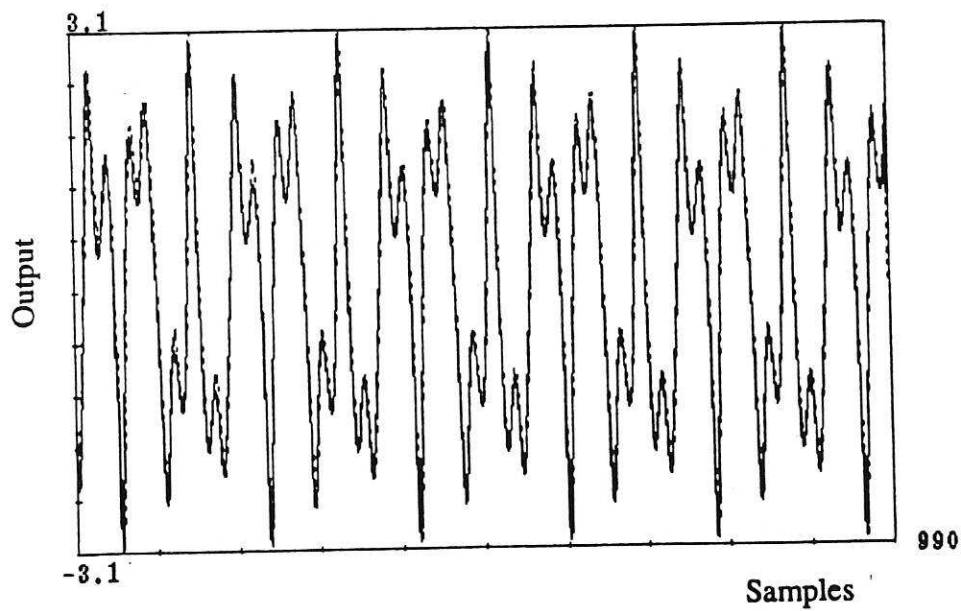
Figure 9b. (...) Measured output and (—) predicted output - $T = \pi/30$
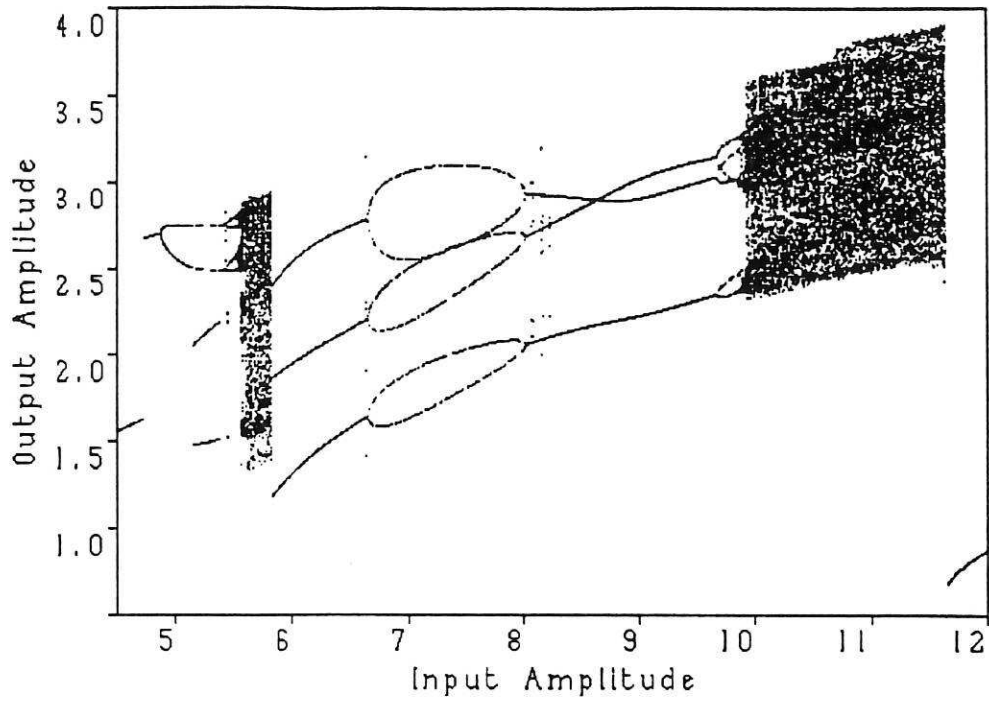
Figure 10a. Bifurcation Diagram — T = π/300
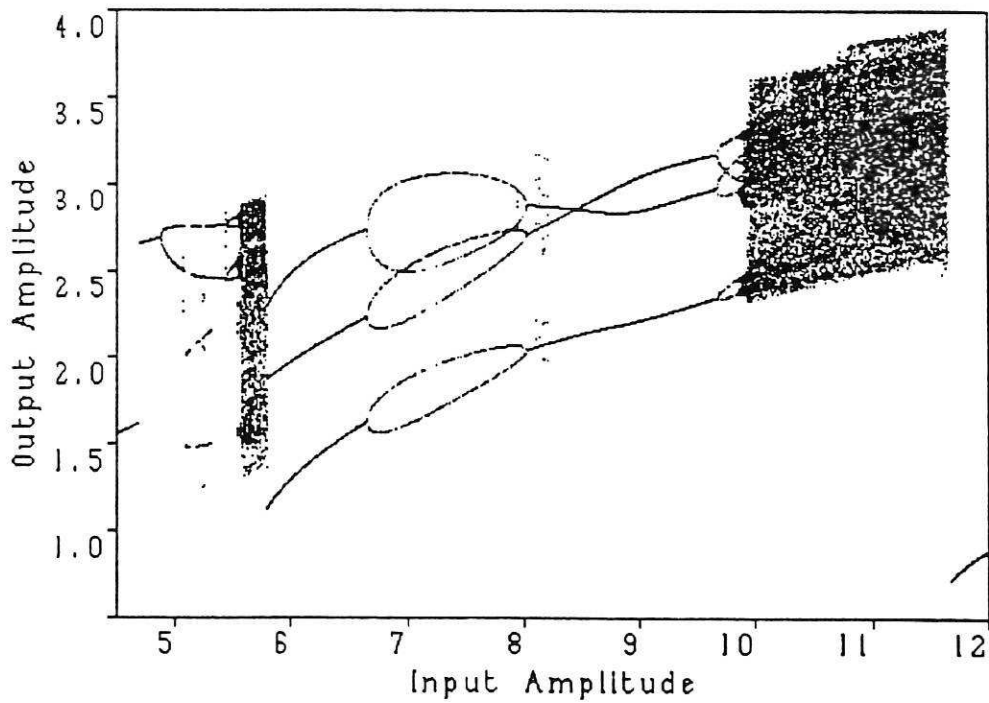
Figure 10b. Bifurcation Diagram — T = π/60
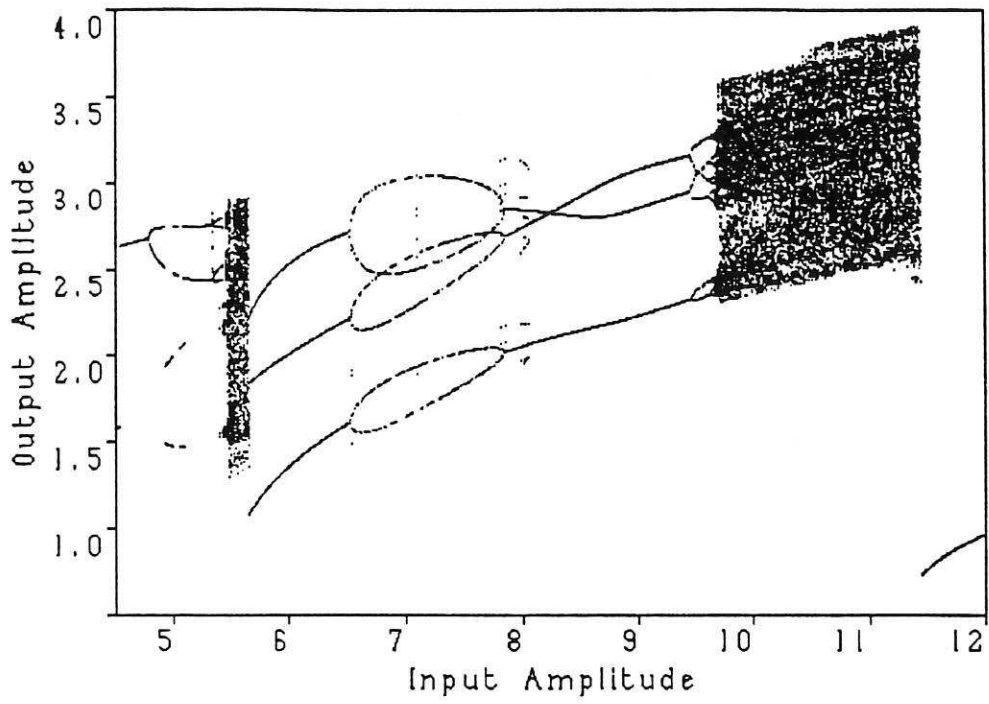
Figure 10c. Bifurcation Diagram - T = π/30
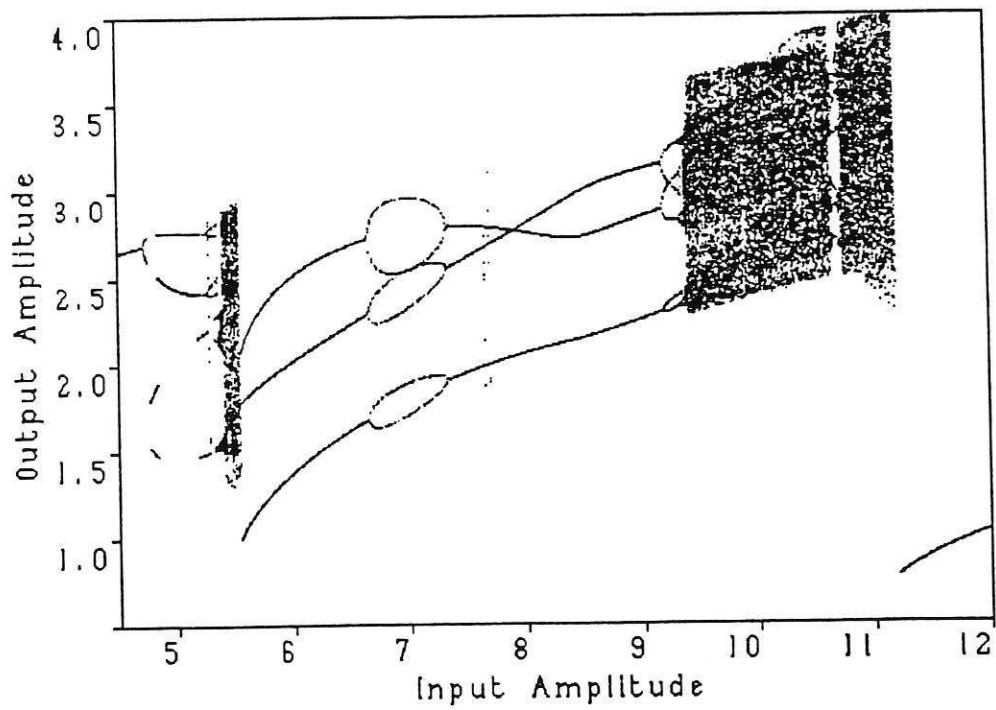
Figure 10d. Bifurcation Diagram - T = π/15
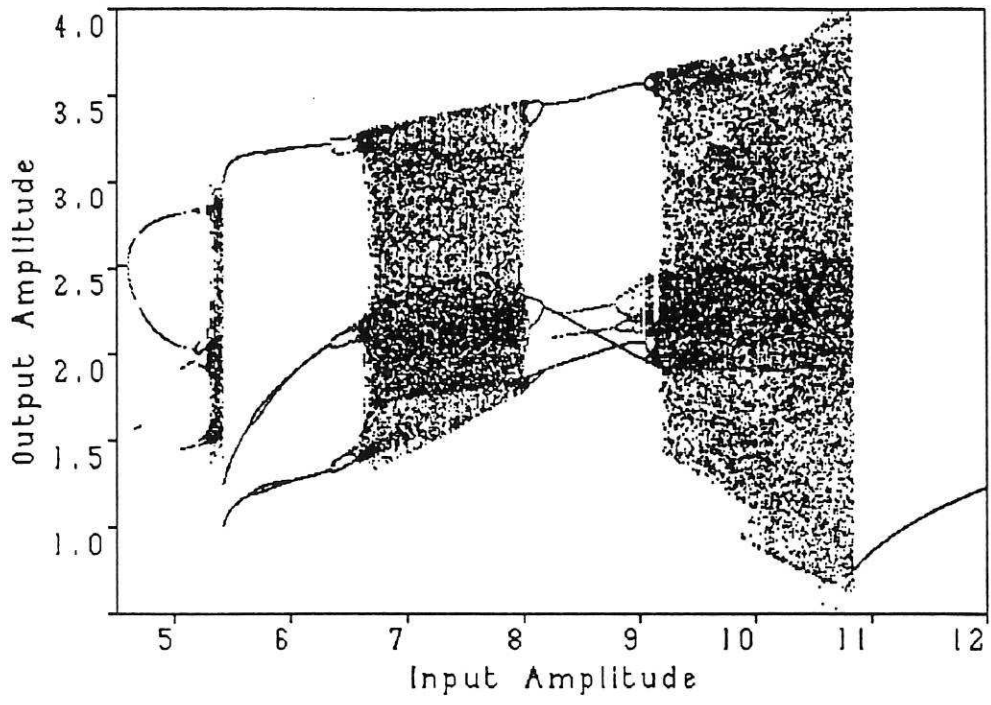
Figure 10e. Bifurcation Diagram — T = Π/12.5
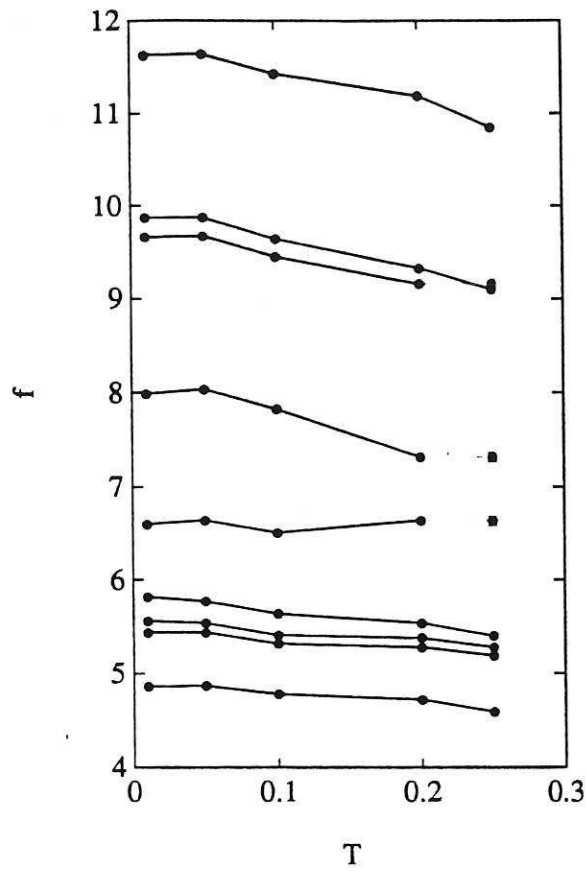
Figure 11. Influence of T on the bifurcation points
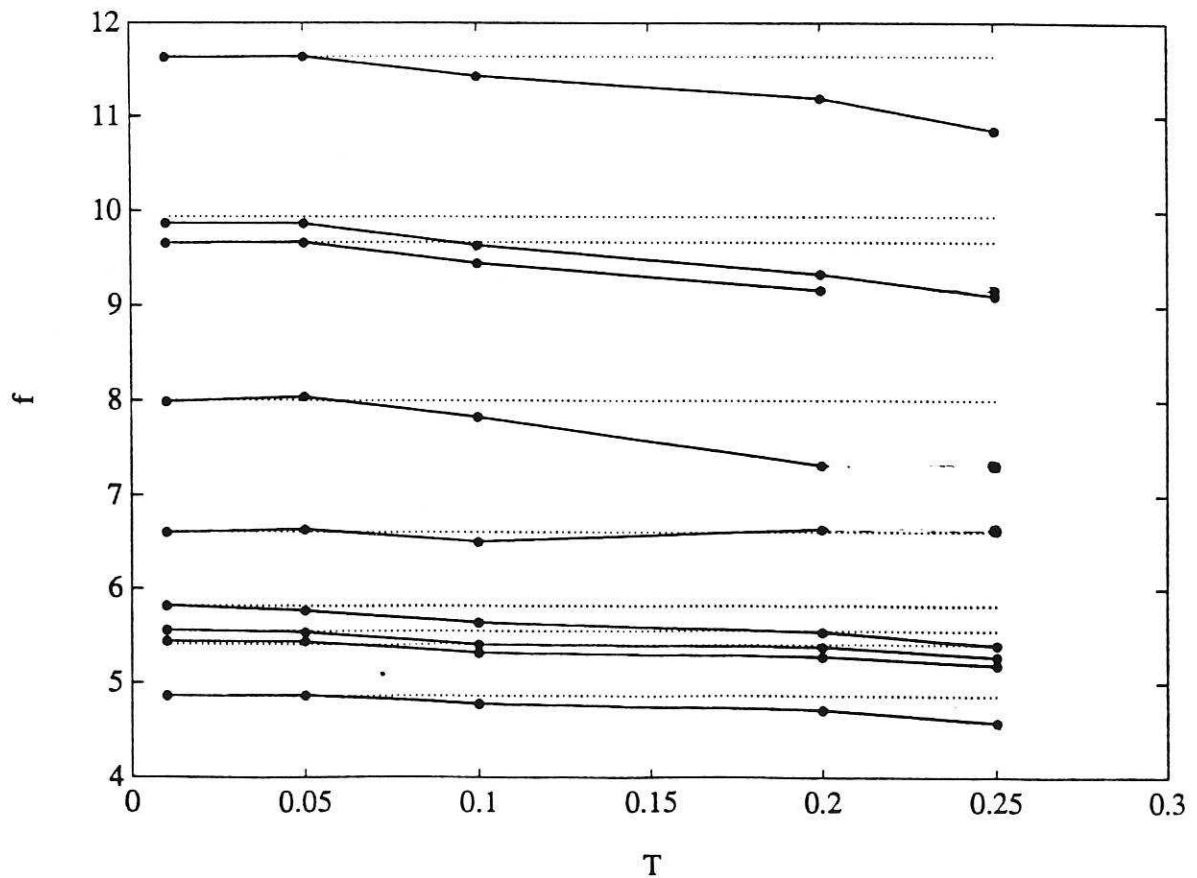
Figure 12. (—) Bifurcation points of the discretised models and (...) bifurcation points of (1) simulated with $\Delta t = \pi/3000$
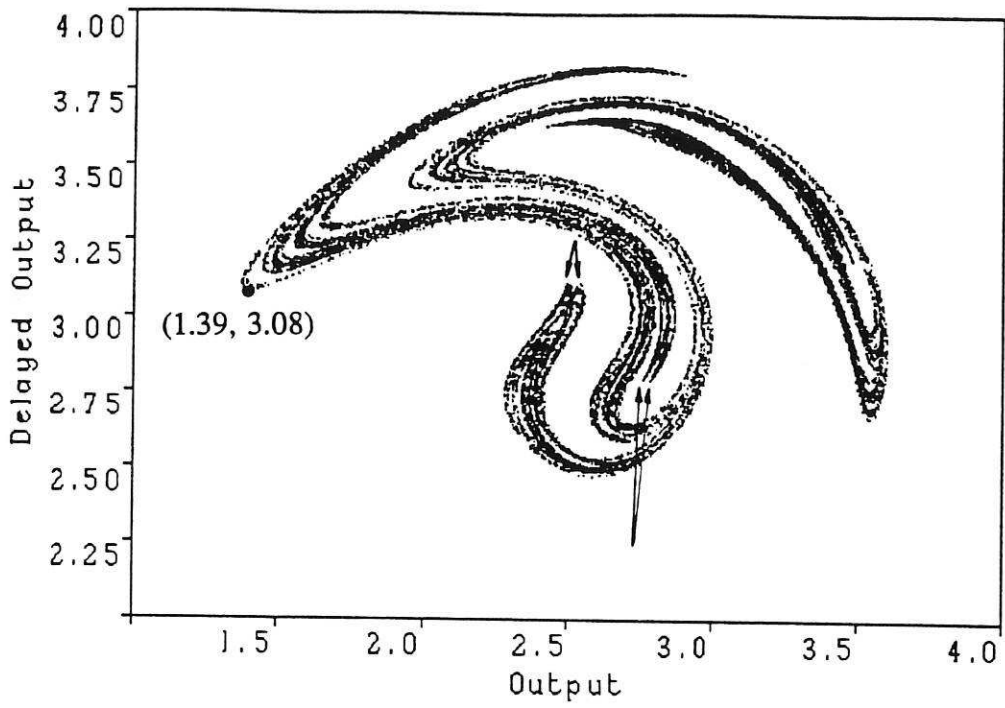
Figure 13a.   Poincaré Map — T = π/300
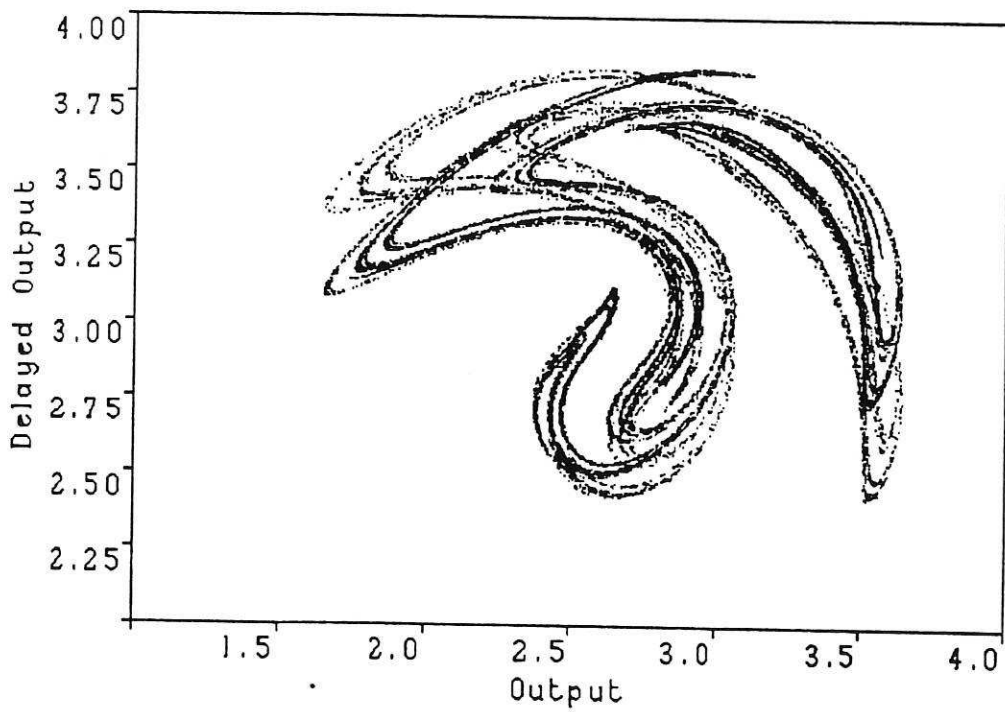

Figure 13b.   Poincaré Map — T = π/60
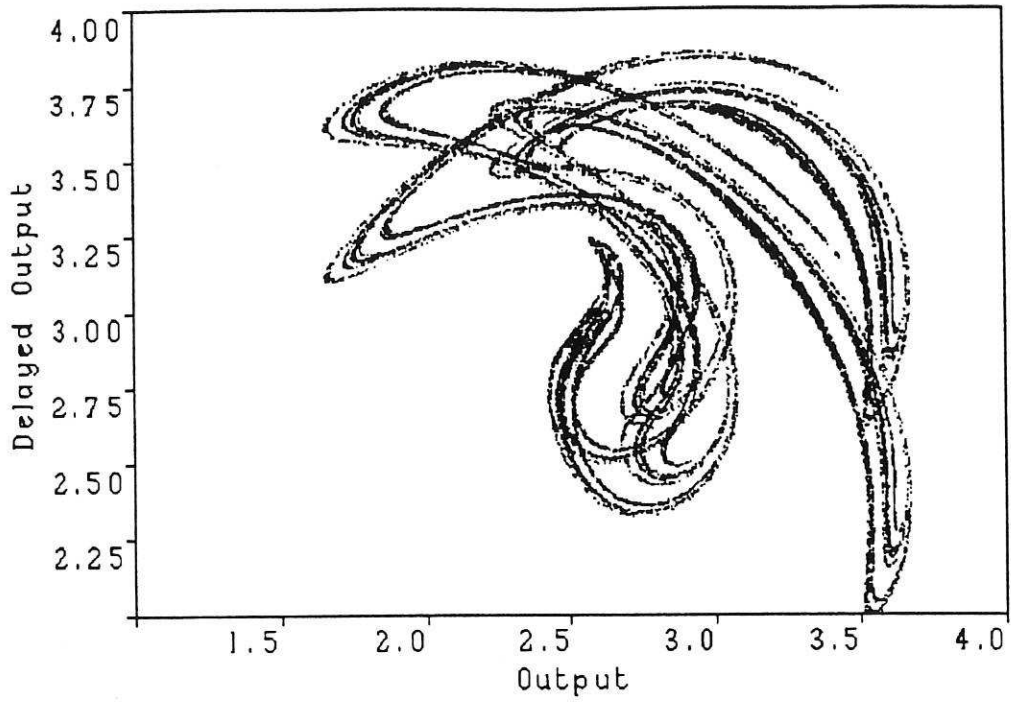
Figure 13c.   Poincaré Map – T = $\pi/30$
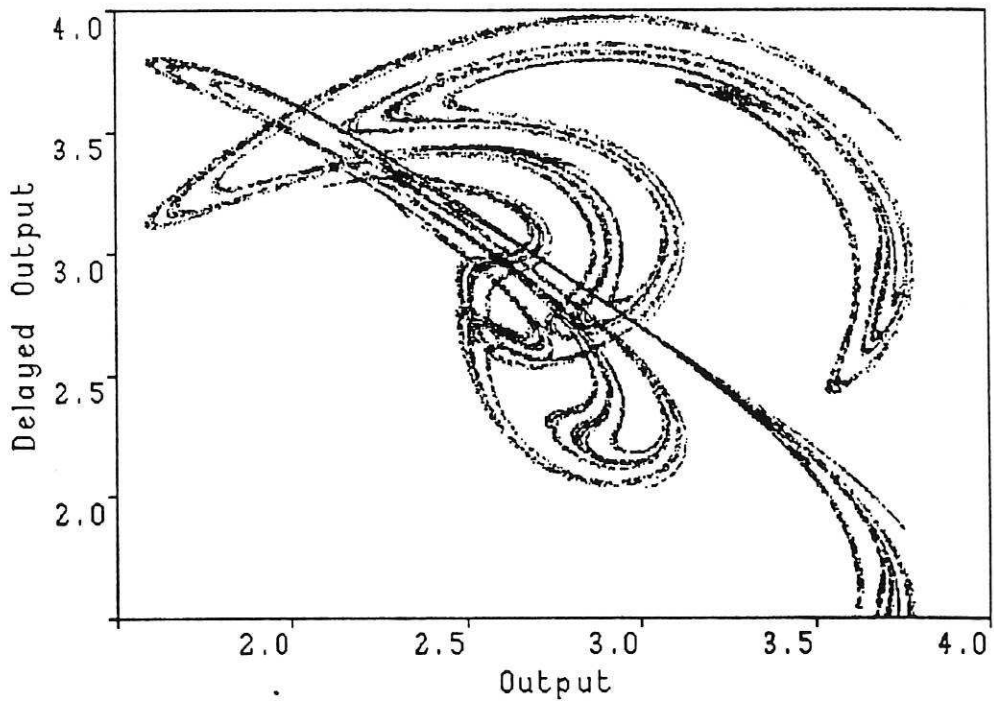
Figure 13d.   Poincaré Map – T = $\pi/15$
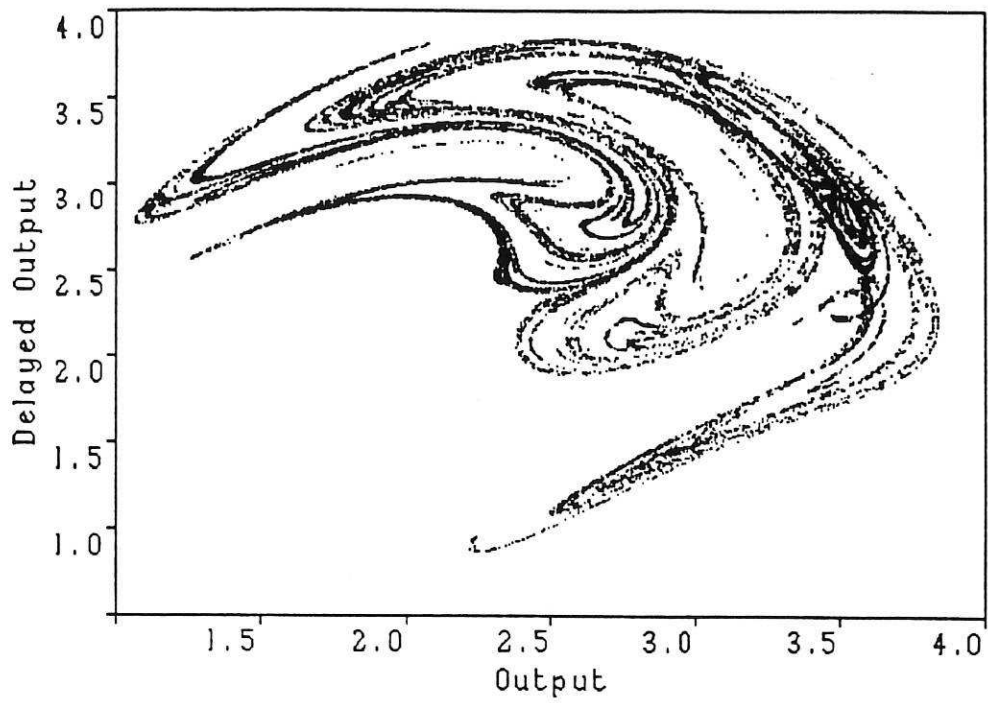
Figure 13e.   Poincaré Map — T = $\pi/12.5$
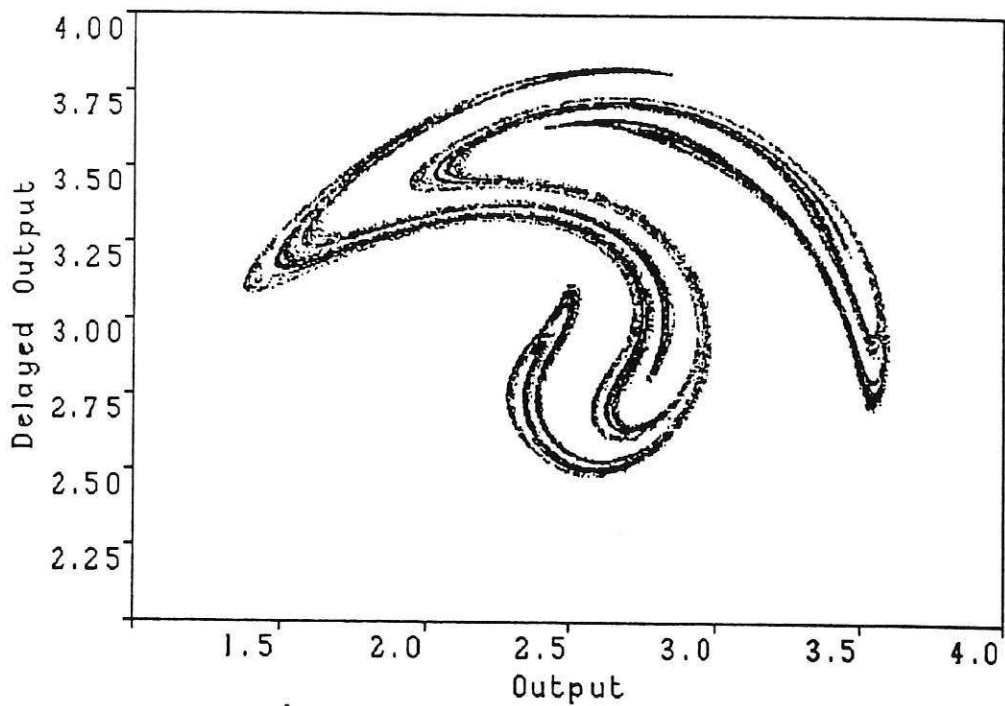

Figure 14.   Poincaré Map — T = $\pi/600$